Axial Mass Transfer in Taylor Flow through Circular Microchannels

Wael Salman, Asterios Gavriilidis, and Panagiota Angeli
Dept. of Chemical Engineering, University College London, Torrington Place, London WC1E 7JE, U.K.

DOI 10.1002/aic.11148
Published online May 1, 2007 in Wiley InterScience (www.interscience.wiley.com).

A Computational Fluid Dynamics (CFD) model has been formulated to evaluate axial mixing in Taylor flow. The residence-time distribution (RTD) curves of a Taylor flow unit cell (comprised of a liquid slug and two half bubbles) is calculated numerically from a step-tracer simulation by solving the steady-state Navier-Stokes and the transient convection-diffusion equations for a variety of conditions ($10 < Pe < 10^5$, $10^{-5} < Ca < 10^{-3}$). The concentration calculated at the outlet of a unit cell gives the cell-density function, from which its RTD curve can be found. Two different trends in the unit cell RTD curves were observed with Pe. At high Pe, the curves have characteristic peaks, while at low Pe only one peak is found that decays slowly. The size and separation of the peaks is affected by the Pe, film thickness $\bar{\delta}$, and slug length, but not Re. The moments of the RTD curves are then used to assess literature unit cell models (CSTR-PFR, two-region, and the model of Thulasidas et al.[1]) For $Pe\bar{\delta} > 10$ the CSTR-PFR model showed the largest difference from the CFD simulations, while the model by Thulasidas et al. showed reasonable agreement. The two-region model fitted the simulations, but only for Sh values significantly different from those found by literature correlations. For $Pe\bar{\delta} < 10$, the CSTR-PFR model gave the best predictions compared to the numerical simulations. A method for calculating the residence-time distribution of a reactor, based on the residence-time distribution of a unit cell by means of a convolution method, was also introduced and gave results which compared very well with experimental data. The short length of the reactor used in the experiments, however, could not allow proper differentiation from other models investigated, which also showed good agreement with the experimental data.
 AIChE J, 53: 1413–1428, 2007
Keywords: Taylor flow, dispersion, axial mixing

Introduction

Taylor flow is one of the dominant gas-liquid flow patterns in microscale diameter channels. It consists of elongated gas bubbles of equivalent diameter larger than the channel diameter separated by liquid slugs. The bubbles adopt a characteristic capsular shape. They almost completely fill the channel cross section, and are only separated from the wall by a thin film of liquid. Because of the presence of bubbles in front and at the back of the slugs, the flow field in the liquid is modified compared to single-phase flow, and toroidal vortices are formed.[2]

Compared to single-phase laminar flow, Taylor flow offers many advantages.[3] Because the bulk liquid is separated by the gas bubbles, axial mixing between the liquid slugs is significantly reduced. The film surrounding the bubbles is the only means of communication between two successive slugs, and in the majority of cases its thickness is only a fraction of a percentage of the tube diameter. Also within the slugs the recirculation of the liquid improves radial mass transfer, that is, from gas to liquid and from liquid to wall.[4–6]

Correspondence concerning this article should be addressed to P. Angeli at p.angeli@ucl.ac.uk.

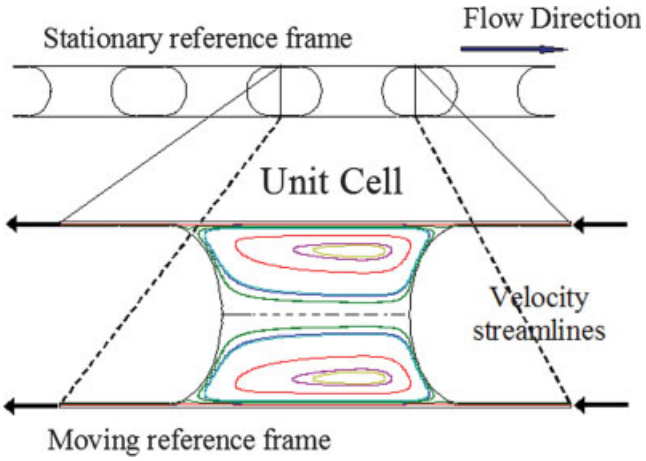

Figure 1. Moving unit cells through a reactor channel appear, when viewed from a frame of reference moving with the velocity of the bubbles, as a small vessel with one inlet and one outlet.

The flow patterns inside the slug are patterns typical for the small *Ca* involved in microreactor applications. [Color figure can be viewed in the online issue, which is available at www.interscience.wiley.com.]

The combination of good radial mass transfer and low-axial mass transfer in the liquid makes Taylor flow suitable for two-phase applications, that involve mass transfer (fluid-fluid or wall-fluid) or single-phase liquid applications which suffer from large back-mixing. For example, the efficiency of many devices like tubular reactors, tubes with absorbing wall for liquid chromatography, and tubular dialysers can be improved by operating them in Taylor flow rather than in single phase.[7] A lot of information on Taylor flow originates from the investigation and characterization of the monolith froth reactor (MFR), where the two fluid phases are introduced into the reactor as froth flow, and pass through the catalyst coated channels in Taylor flow pattern.[1,8,9] The residence time of the liquid in the reactor affects the conversion and selectivity of such systems. Applications of Taylor flow can also be seen in the field of microfluidics, where the introduction of a second immiscible phase was used to improve mixing in the liquid slug, segment the flow and reduce axial mixing.[10–12] In some studies the active reagents were actually introduced into the Taylor drop in order to be kept separate within the microreactor channel.[13]

In the past the low-axial mixing properties of Taylor flow were used in automated analyzers,[14] where the different samples in the feed line should be kept separate. Similarly, an envisaged application of Taylor flow is in high-throughput screening as a means of introducing sequentially different reactants/samples within a microchannel reactor/analyzer. The enhanced heat- and mass-transfer rates possible in microchannels would enable a kinetically controlled operating regime to be established that allows the calculation of reaction kinetics. For such applications it is important to be able to predict the extent of axial mixing and residence-time distribution as a function of the hydrodynamics of the two-phase flow.

This article aims to develop a numerical method based on Computational Fluid Dynamics (CFD) for accurately calculating the residence-time distribution in a Taylor flow tubular system operating in laminar flow. Using this method benchmark cases covering a large range of parameter variations are investigated. The results obtained are also compared with the predictions of previously developed models that were based on simplified assumptions of the flow field in the liquid phase.

Theory and Literature Review

During Taylor flow in microchannels, strong interfacial forces, as well as the contacting at the inlet and separation at the outlet of the two phases may cause pulsation of the flow or a distribution of bubble and slug sizes.[15] The existence of a liquid film surrounding the bubbles depends on the wall surface and liquid properties, as well as on the operating conditions.[15,16] In this article Taylor flow is assumed to be regular (nonpulsating) and periodic (no variation in bubble or slug sizes) in agreement with the wider body of literature on this flow pattern in small tubes. The description of small implies the dominance of surface tension over gravity forces. Various criteria can be found in literature to indicate when this happens. The criterion used here is $(\rho g d^2/\gamma) \lesssim 3.37$, based on the work by Bretherton.[17] In addition, there is negligible flow in the liquid film surrounding the bubbles and the geometry of the bubble is axisymmetric.

In periodic Taylor flow, a single period consists of a bubble and a slug, or a slug and two half bubbles, usually referred to as a *unit cell*. The unit cell moves with the velocity of the bubble, which is faster than the average liquid velocity in the slug, because of the presence of the near stagnant liquid film separating the bubble from the wall. A moving unit cell, seen from a frame of reference moving with the bubble resembles a reactor with one inlet and one outlet (Figure 1).

Following the pulsed tracer experimental methodology for determining the residence-time distribution curve,[18] a tracer is conceptually introduced at time zero into a Taylor flow reactor of length $l_{reactor}$, such that it fills (and is only confined to) a single unit cell (see Figure 2a). The amount of tracer material introduced into the channel is calculated from the product of the tracer concentration and the liquid slug volume. As the tracer cell moves through the reactor some tracer is communicated upstream through the film into the next cell that enters the reactor. When the whole of cell 2 is

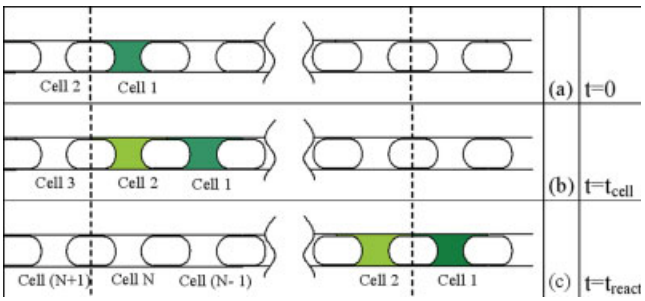

Figure 2. Method of acquiring the residence-time distribution curve.

The boundaries of the reactor are denoted by the dashed vertical lines. [Color figure can be viewed in the online issue, which is available at www.interscience.wiley.com.]

in the reactor the time passed is $t_{cell} = l_{cell}/U_b$, (see Figure 2b). The process continues as more cells enter the reactor, and each cell experiences at its inlet the tracer that the downstream cell deposits behind. When cell 1 completely exits the reactor, its residence time in the reactor is $t_{reactor} = l_{reactor}/U_b$, see Figure 2c. The concentration of the exiting slug is averaged and noted as the reactor outlet concentration for time interval $t_{reactor} - t_{cell} \leq t \leq t_{reactor}$.

Determining the output and internal concentration of a unit cell for a given time-varying tracer input is the next step. Under certain assumptions, the outlet concentration can be predicted analytically. Thiers et al.[19] assumed perfect mixing in the slugs obtaining a tank-in-series model. In another article, Salman et al.[20] have restricted the assumption of perfect mixing to low Peclet numbers ($Pe < 500$), and used a CSTR-PFR in series model to predict the response of the unit cell. It was further shown that for very low Peclet numbers, forward axial mixing, as well as axial backmixing occurs, and this was accounted for by incorporating diffusion in the PFR equation in the CSTR-PFR model.

In more sophisticated models, the region of the slug can be divided into two separate regions; a closed vortex region where the recirculation occurs, and an enclosing open thin liquid annulus region (Figure 1). This division is the basis of two-region models. Pedersen and Hovarth[21] proposed a two-region model where the two regions (the film and the vortex) are assumed to be well mixed, and a mass-transfer coefficient is used to account for mass transfer between them. They obtained this parameter from studies of slug to wall mass-transfer coefficients.[22] Average mass-transfer coefficients can also be found in other sources.[5,6,8,23] Thulasidas et al.[1] assumed the same two regions of the liquid slug to be well mixed in the axial direction, and exchange mass only by diffusion in the radial direction. A one-dimensional (1-D) transient-diffusion equation, and an averaging procedure were then used to calculate the mass transfer. Starting with an initial concentration in the annulus region and in the core circulation region, the equation is solved for a time equivalent to that of a single circulation cycle, then the concentrations of the two regions are averaged. This average core concentration is then used as an initial condition for the next solution, while the average concentration in the annulus region is the output response of the unit cell for the duration of the solved time. Kreutzer[8] developed a "continuous multizone model" version of the two-region model of Pedersen and Hovarth,[21] with the discrete unit cell approximated by a differential element.

Pedersen and Hovarth[21] used convolution methods to obtain from the residence-time distribution in a single unit cell, the residence-time distribution of the whole Taylor flow channel. Pedersen and Hovarth,[21] Thulasidas et al.[1] and Kreutzer[8] compared the reactor residence-time distribution curves calculated from their models with experimental ones to validate the single-cell models. One of the aims of this work is to provide accurate simulated residence-time distribution data of unit cells against which previous models can be directly compared.

Model Theory

To totally account for the hydrodynamics during gas-liquid Taylor flow, bubble shapes and velocity, film thickness and flow field in the liquid slugs need to be known. The governing dimensionless parameters derived from the Navier-Stokes equations and boundary conditions for a gas-liquid Taylor flow are given in Table 1.

Table 1. Dimensionless Numbers Governing the Hydrodynamics of Taylor Flow[24]

Dimensionless Number	Definition
Ca	$\mu U_b/\gamma$
Fr	U_b^2/gd
L_b	l_b/d
L_s	l_s/d
Re	$\rho U_b d/\mu$

Many numerical studies have been conducted to determine the influence of these parameters on the flow.[24–27] In general the effect of increasing Ca is always to increase the thickness of the liquid film surrounding the bubbles. The flow pattern inside long slugs soon attains a parabolic profile away from the bubble caps for sufficiently long L_s. For $Ca < 10^{-3}$, the shapes of the bubble caps can be assumed spherical, and the annular film reaches terminal film thickness quickly so that the body of the bubble can be approximated by a cylinder. The increase in Re causes an increase in the slug length necessary for a parabolic flow profile to develop. Re has limited effect on the shape of the bubble and film thickness for $Ca < 10^{-3}$.[24] While the bubble length L_b has been shown to affect the terminal velocity of the bubble when it is smaller than a certain minimum length which depends on Re and Ca, it is only for the cases where $Ca > 10^{-3}$ that this is significant.[28] In practice L_b needs to be made sufficiently large ($L_b \gtrsim 1.2$) for a constant film thickness to be reached. Fr influences the amount of liquid flowing in the falling film surrounding the bubbles in vertical arrangements. The influence of increasing Fr is to increase the bubble velocity. In general, the effects of Re, L_b and Fr can be neglected for $Ca \leq 10^{-3}$.[24]

The dominance of surface forces in small diameter channels brings to prominence the effect of contaminant surface active agents. Their presence usually results in a larger film thickness than predicted by theory and modifications to the flow field. The characterization of such effects requires the introduction of many more parameters (surfactant interface adsorption/desorption rates and interface diffusivity),[29] which vary from system to system and are very difficult to measure or estimate (the most measurable effect is on the terminal film thickness). Depending on the nature and concentration of surfactants, the nature of relation between Ca and film thickness $\bar{\delta}$ is modified. As a result, it is better to use the film thickness $\bar{\delta}$ as a parameter than Ca. The change in the flow field with trace contaminant surfactant also depends on the effect of the contaminants on the surface tension and the actual contaminant concentration.[29] To facilitate the current analysis, it is assumed that the concentrations of the contaminants are such that the effects on the flow field in the liquid are negligibly small.

Although the different dimensionless parameters are independent, once a specific system is selected all the physical constants are fixed, and the parameters are linked by the tube diameter and the bubble velocity. Considering the properties

Table 2. Range of Dimensionless Numbers Considered in this Work

Ca	δ/d	$Re_{\min}$	$Re_{\max}$	$Pe_{\min}$	$Pe_{\max}$
10^{-3}	6.36×10^{-3}	4.95×10^{-5}	3.09×10^{2}	3.70	1.78×10^{6}
10^{-4}	1.41×10^{-3}	4.95×10^{-5}	3.09×10^{1}	3.70	1.78×10^{5}
10^{-5}	3.06×10^{-4}	4.95×10^{-5}	3.09	3.70	1.78×10^{4}
10^{-6}	6.60×10^{-5}	4.95×10^{-5}	3.09×10^{-1}	3.70	1.78×10^{3}

of many common solvents and a range of $10^{-6} \leq Ca \leq 10^{-3}$ (deduced from tube lengths, diameters and reaction-residence times which could be encountered in microreactor engineering applications), the ranges of other dimensionless numbers were calculated (Table 2). The limits on Peclet number were deduced for diffusivities $5 \times 10^{-11} \leq D \leq 10^{-8}$ m^2/s, which are typical of many materials in water.[30] The lower limit corresponds to diffusivities of large molecules.

Problem formulation and solution method for unit cell

For the range $10^{-6} \leq Ca \leq 10^{-3}$ bubbles are well approximated by a cylinder with spherical cap ends. Film thickness range was estimated from correlations in terms of Ca.[24] As explained in the previous section the results will be reported in terms of film thickness rather than Ca. Dimensionless slug lengths were taken as $L_s = \left\{\frac{1}{4}, 1, 4\right\}$, based on previous experimental work.[15] The upper limit did not exceed 4 because the mass transfer performance of Taylor reactors worsens with increased slug lengths.[20,23] Liquid films surrounding bubbles are generally thin and well mixed radially. In general, they can be approximated as plug-flow reactors (PFR), whose only effect is to delay the signal output of a step pulse input. The effect of increasing bubble length would be a shift to the right in the time axis of the residence-time distribution curve. As a result, only a single bubble length, approximated by $L_b \simeq 1.1$, was used in all simulations.

The first step in the solution method was to obtain the flow field in the liquid slug between two consecutive bubbles (see for example Figure 1). This was calculated by solving the Navier-Stokes Eq. 1 for that geometry (shown in Figure 3). The characteristic quantities used in the nondimensionalization of the equations and boundary conditions are given in Table 3.

$$Re\ \bar{\mathbf{u}} \cdot \overline{\nabla}\bar{\mathbf{u}} = -\overline{\nabla}\bar{p} + \overline{\nabla}^2 \cdot \bar{\mathbf{u}} \tag{1}$$

The boundary conditions are given in Table 4. To solve Eq. 1, a commercial finite element software package, Femlab® by Comsol is used. Standard second-order elements were used for the velocity fields, and first-order elements for the pressure field. The total number of elements varied between 2,851 and 11,270, with the larger number of elements used for the larger L_s. There was a larger concentration of elements near the bubble caps and at the boundary between the liquid film and the vortex region. Sensitivity studies were carried out to ensure grid independence of the resulting flow field.

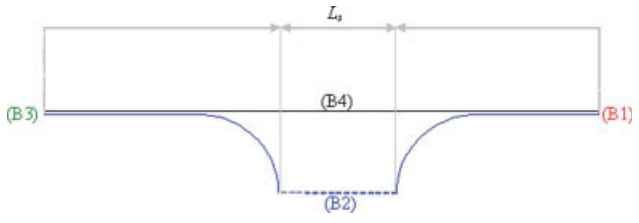

Figure 3. Geometry and boundaries of the computational domain.

[Color figure can be viewed in the online issue, which is available at www.interscience.wiley.com.]

Table 3. Characteristic Quantities used in Dimensionless Variables

Velocity	U_b, velocity of the bubble
Length	d, tube diameter
Time	d/U_b
Concentration	c_i, constant inlet concentration

The second step of the solution method was to solve the convection-diffusion Eq. 2 with boundary conditions given by Table 5 with Femlab, using a similar computational domain as that used for the hydrodynamics (see Figure 3)

$$\frac{\partial \bar{c}}{\partial \bar{t}} + \bar{\mathbf{u}} \cdot \overline{\nabla}\bar{c} - \left(\frac{1}{Pe}\right)\overline{\nabla}^2\bar{c} = 0 \tag{2}$$

The velocity field $\bar{\mathbf{u}}$ used in the equation is that calculated in step 1. The initial condition of the tracer in the computational domain is constant concentration of $\bar{c} = 0$. The output concentration at boundary (B3) at regular time-steps was calculated from the average flux over the cross section.

Third-order elements were used for the concentration of the tracer. Their number varied from 5,620 to 15,431. The numerics of the simulation limited the values of Peclet number which could be used. Beyond Pe of the order of 10^5 significant overshooting (concentration in excess of the maximum concentration of 1) and undershooting (negative concentrations) develop around areas of high-concentration gradients (specifically in the region of the stream line separating the film and the circulation area). While these can be treated using various shock capturing techniques[31] they introduce artificial diffusion, and for that reason were not used. Therefore, the upper limit considered was $Pe = 10^5$, and even for that limit some shock effects are observed during the early stages of the simulation which did not disappear with local grid refinements. The overshoot/undershoot in dimensionless concentration was localized, and of a value less than ± 0.08, which disappears as the concentration gradients reduced with time.

The solution of hydrodynamics and convection-diffusion equations was carried out using an Athlon 1.6GHz processor with 1Gb RAM. The hydrodynamic solution is easily obtained in $\sim$ 8 min of CPU time. The concentration at the output of the unit cell for the time-dependent solution of the

Table 4. Boundary conditions used for the Navier-Stokes Eq. 1

(B1) Inlet	$\bar{u}_z = -1, \bar{u}_r = 0$
(B2) Slip or symmetry	$\mathbf{n}_b \cdot \bar{\mathbf{u}} = 0, \frac{\partial \bar{\mathbf{u}}}{\partial n} = 0$
(B3) Straight-out condition	$\mathbf{n}_t \cdot \bar{\mathbf{u}} = 0, \bar{p} = 0$
(B4) Wall	$\bar{u}_z = -1, \bar{u}_r = 0$

Table 5. Boundary Conditions used for the Convection Diffusion Eq. 2

(B1) $\bar{c}_i = 1$
(B2) $\mathbf{N} \cdot \mathbf{n}_b = 0$
(B3) $\mathbf{N} \cdot \mathbf{n}_b = c\bar{\mathbf{u}} \cdot \mathbf{n}_b$
(B4) $\mathbf{N} \cdot \mathbf{n}_b = 0$

convection-diffusion Eq. 2, was evaluated in less than 10 stages. Initially, output concentrations were stored at time-steps $\Delta\bar{t} = 0.1$. Then, the storage steps were increased in stages. $\Delta\bar{t} = 100$ was the maximum time-step size used to resolve the long tail of the distribution for some systems. The CPU time required for the initial stage was longest (maximum $\sim$ 8 h for the highest Pe) but dropped to $\sim$ 7 min for the later stages.

Residence-time distribution of unit cell

The concentration at the outlet of a unit cell $\bar{c}_o(\bar{t})$ in response to a step input gives the density function $F(\bar{t})$. This output is calculated for all time-steps, and an interpolation using natural cubic splines of this data corresponds to the continuous function $F(\bar{t})$. The equation of the natural cubic spline function for a set of numerical data obtained at times $\{\bar{t}_1, \bar{t}_2, \ldots, \bar{t}_n\}$, can be written as

$$\begin{aligned} Sp(\bar{t}) &= \alpha_1 + \beta_1(\bar{t}-\bar{t}_1) + \varepsilon_1(\bar{t}-\bar{t}_1)^2 + \phi_1(\bar{t}-\bar{t}_1)^3 \quad \text{for } \bar{t}_1 \le \bar{t} \le \bar{t}_2 \\ &= \alpha_2 + \beta_2(\bar{t}-\bar{t}_2) + \varepsilon_2(\bar{t}-\bar{t}_2)^2 + \phi_2(\bar{t}-\bar{t}_2)^3 \quad \text{for } \bar{t}_2 \le \bar{t} \le \bar{t}_3 \\ &: \\ &= \alpha_{n-1} + \beta_{n-1}(\bar{t}-\bar{t}_{n-1}) + \varepsilon_{n-1}(\bar{t}-\bar{t}_{n-1})^2 + \phi_{n-1}(\bar{t}-\bar{t}_{n-1})^3 \quad \text{for } \bar{t}_{n-1} \le \bar{t} \le \bar{t}_n \end{aligned} \tag{3}$$

The spline coefficients were calculated using an adaptation of the method by Burden et al.[32] in Mathematic®.[33] Splines were used in the interpolation because they have continuous first and second derivatives. The derivative of $F(\bar{t})$ with respect to time gives the residence-time distribution curve $E(\bar{t})$. The process of differentiating the data introduces spurious errors specifically around areas where there is a sharp change in the gradient of $F(\bar{t})$, and not enough sampling points. With that in mind the curves obtained for the residence-time distributions $E(\bar{t})$ still produced useful information.

Once the unit cell residence-time distribution curves are obtained, their moments are calculated up to the third one to characterize them. Moments are easy to calculate using Eq. 4, however, with increasing moment order larger errors are introduced in their calculation[18]

$$\bar{\mu}_n = n\int_0^\infty \bar{t}^{n-1}[1 - F(\bar{t})]d\bar{t} \tag{4}$$

$$\bar{\sigma}^2 = \bar{\mu}_2 - \bar{\mu}_1^2 \tag{5}$$

The models used to describe the behavior of the unit cell in literature, usually have at most a single adjustable parameter, which accounts for the incomplete knowledge of the mixing process in the liquid slug. This parameter is determined for unit cells by comparing the model predictions against experimental data for the whole reactor, and picking a value for the parameter so that the model best matches the data according to certain criteria. In this work, literature models for a single unit cell are fitted to the numerical data obtained from the simulations. Two steps are necessary: first assess/obtain the fitting parameter, and then compare the quality of the fit with the original numerical data.

Two possible procedures are available for fitting and comparing the quality of the fit, as discussed by Nauman and Buffham.[18] In the method of moments, the n parameters are fitted to satisfy the first n moments, and the quality is assessed by considering the value of the $n + 1$ moment. The second method is to use a fitting algorithm where the parameters of a model are fitted so as to minimize the square of the difference between the data and the model (Eq. 6).

$$\text{square error} = \int_0^\infty (F_{model}(\bar{t}) - F(\bar{t}))^2 d\bar{t} \tag{6}$$

In this work, the second method is used as it was found difficult to make a qualitative judgement on the quality of the fit based on the values of moments. Nevertheless, the values of the moments are also reported because they can easily be used to estimate adjustable parameters and make comparisons between different models without recourse to the RTD data.

Residence-time distribution of reactor

Using simple conservation of mass arguments, the average concentration $\bar{c}_{av}$ inside a slug in dimensionless form can be given by Eq. 7.

$$\frac{d\bar{c}_{av}(\bar{t})}{d\bar{t}} = \frac{A_f}{V}\frac{d}{}(\bar{c}_i(\bar{t}) - \bar{c}_o(\bar{t})) \tag{7}$$

where $\bar{c}_i$ and $\bar{c}_o$ are the dimensionless inflow and outflow concentrations respectively.

The Laplace-transform of the earlier expression is

$$\bar{s}\,\bar{C}_{av}(\bar{s}) - \bar{c}_{av}(0) = \frac{A_f}{V}\frac{d}{}(\bar{C}_i(\bar{s}) - \bar{C}_o(\bar{s})) \tag{8}$$

A slug of zero initial concentration $\bar{c}_{av}(0) = 0$ experiencing an input $\bar{C}_i(\bar{s})$, gives an output $\bar{C}_o(\bar{s}) = E(\bar{s})\bar{C}_i(\bar{s})$, where $E(\bar{s})$ is the Laplace transform of the residence-time distribution function of a single unit cell. This can be substituted in Eq. 8 to give

$$\bar{C}_{av}(\bar{s}) = \frac{A_f}{V}\frac{d}{}\frac{\bar{C}_i(\bar{s})(1 - E(\bar{s}))}{\bar{s}} \tag{9}$$

The first slug needs to be considered differently, because it has unit concentration and experiences a 0 input concentration (see Figure 2(a). It can be shown that the output of the first slug is given by $\overline{C}_o^1(\bar{s}) = ((1 - E(\bar{s}))/\bar{s})$, and from Eq. 8, $\overline{C}_{av}^1(\bar{s}) = \frac{1}{\bar{s}} - ((A_f\ d)/V)((1 - E(\bar{s}))/\bar{s}^2)$. Output and average concentration of slugs in the Laplace domain are given in Table 6.

Once the unit cell $F(\bar{t})$ is known numerically from CFD, the $F(\bar{s})$ is calculated by applying the Laplace transform to the corresponding spline polynomials fitting the numerical data. The Laplace transform of the interpolated function $F(\bar{t})$, with N data points is given by Eq. 10.

$$F(\bar{s}) = \mathcal{L}(F(\bar{t})) = \sum_{n=1}^{N}\left[\frac{e^{-\bar{s}\bar{t}_{n-1}} - e^{-\bar{s}\bar{t}_n}}{\bar{s}}\right]\alpha_{n-1} + \left[\frac{(e^{-\bar{s}\bar{t}_{n-1}} - e^{-\bar{s}\bar{t}_n})}{\bar{s}^2} - \frac{(\bar{t}_n - \bar{t}_{n-1})e^{-\bar{s}\bar{t}_n}}{\bar{s}}\right]\beta_{n-1} + \left[\frac{2(e^{-\bar{s}\bar{t}_{n-1}} - e^{-\bar{s}\bar{t}_n})}{\bar{s}^3} - \frac{2e^{-\bar{s}\bar{t}_n}(\bar{t}_n - \bar{t}_{n-1})}{\bar{s}^2} - \frac{e^{-\bar{s}\bar{t}_n}(\bar{t}_n - \bar{t}_{n-1})^2}{\bar{s}}\right]\varepsilon_{n-1} + \left[\frac{6(e^{-\bar{s}\bar{t}_{n-1}} - e^{-\bar{s}\bar{t}_n})}{\bar{s}^4} - \frac{6e^{-\bar{s}\bar{t}_n}(\bar{t}_n - \bar{t}_{n-1})}{\bar{s}^3} - \frac{3e^{-\bar{s}\bar{t}_n}(\bar{t}_n - \bar{t}_{n-1})^2}{\bar{s}^2} - \frac{e^{-\bar{s}\bar{t}_n}(\bar{t}_n - \bar{t}_{n-1})^3}{\bar{s}}\right]\phi_{n-1} \quad (10)$$

Next, the Laplace transform of the unit cell RTD curve is calculated from the transform of the density function

$$E(\bar{s}) = \bar{s}F(\bar{s}) + F(0) \quad (11)$$

Following, the expressions of $\bar{C}_{av}^n(\bar{s})$ are calculated from Table 6.

The concentration at the outlet of the reactor is obtained from evaluating the inverse Laplace transform of functions in Table 6 at dimensionless times given by Table 7. Numerical inversion of the Laplace transform is ideal for this type of problem, as the concentrations that need to be evaluated are those of the slugs at the exit of the reactor. There are various known algorithms for this inversion, and the one used in this work is an adaptation of Gaver functionals with Wynn's rho acceleration algorithm[34] as implemented in Mathematica®.[35] From the speed of each unit cell and its length, as well as the length of the reactor, the concentration at different times can be plotted and converted to a reactor residence-time distribution curve $E_{\text{reactor}}(\bar{t})$ when normalized.

Results and Discussion

The solution of the Navier-Stokes equation showed the typical recirculation patterns in the liquid as illustrated in Figure 1. The moments of the unit cell residence-time distribution curves for the different cases studied are summarized in Table 8. The zeroth and first moments are used as a further check for the quality of the numerical solution. The zeroth moment should be equal to one and the first moment should be the space-time of the unit cell calculated simply from expression 12

$$\bar{\tau} = \frac{V}{A_f d} = \frac{\bar{R}(2(\bar{R} - \bar{\delta}) + L_s) - \frac{4}{3}(\bar{R} - \bar{\delta})^3}{2\bar{R}\left(\bar{R}^2 - (\bar{R} - \bar{\delta})^2\right)} + L_b - 2(\bar{R} - \bar{\delta}) \quad (12)$$

It can be seen that all runs with $Pe = 10$ have a considerably lower value of the first moment than the space-time of the unit cell. This is attributed to the breakdown of the assumption that convection dominates mass transfer at the boundaries (closed-closed system assumption is necessary in residence-time distribution analysis). Boundary (B1) is not a closed boundary and diffusion there may account for these results. For low Pe, the approach of Salman et al. is more suitable.[20]

Table 6. Laplace Transforms of the Output and Average Concentration of Slug 'n'

Slug Output Concentration	Slug Average Concentration
$\bar{C}_o^1(\bar{s}) = \left(\frac{1-E(\bar{s})}{\bar{s}}\right)$	$\bar{C}_{av}^1(\bar{s}) = \frac{1}{\bar{s}} - \frac{A_f\ d}{V}\left(\frac{1-E(\bar{s})}{\bar{s}^2}\right)$
$\bar{C}_o^2(\bar{s}) = E(\bar{s})\left(\frac{1-E(\bar{s})}{\bar{s}}\right)$	$\bar{C}_{av}^2(\bar{s}) = \frac{A_f\ d}{V}\left(\frac{1-E(\bar{s})}{\bar{s}}\right)^2$
$\bar{C}_o^3(\bar{s}) = E^2(\bar{s})\left(\frac{1-E(\bar{s})}{\bar{s}}\right)$	$\bar{C}_{av}^3(\bar{s}) = \frac{A_f\ d}{V}\left(\frac{1-E(\bar{s})}{\bar{s}}\right)^2\bar{E}(\bar{s})$
$\bar{C}_o^n(\bar{s}) = E^{n-1}(\bar{s})\left(\frac{1-E(\bar{s})}{\bar{s}}\right)$	$\bar{C}_{av}^n(\bar{s}) = \frac{A_f\ d}{V}\bar{E}^{n-2}(\bar{s})\left(\frac{1-E(\bar{s})}{\bar{s}}\right)^2$

General features of the unit cell RTD/spatial concentration contours, and the effect of the dimensionless parameters

Two distinct types of unit cell concentration patterns are observed, which depend on the Peclet number value. For high-Peclet numbers $\{10^3,\ 10^4,\ 10^5\}$ the contours roughly mirror the streamlines in the liquid. A typical concentration distribution in the slug and corresponding density function $F(\bar{t})$ of the unit cell output are given in Figure 4. Typical features of these curves are:

(1) An initial delay, corresponding to the time for the film to travel across the unit cell.

Table 7. Dimensionless Times $\bar{t}$ where the Inverse Laplace Transforms of $\bar{C}_{av}^n(\bar{t})$ are Calculated

Function	Time for Evaluation
$\mathcal{L}^{-1}\bar{C}_{av}^1(s)$	$L_{reactor}$
$\mathcal{L}^{-1}\bar{C}_{av}^2(s)$	$L_{reactor} + (L_b + L_s)$
:	:
$\mathcal{L}^{-1}\bar{C}_{av}^n(s)$	$L_{reactor} + n(L_b + L_s)$

Note that $\bar{t}$ is equivalent to dimensionless lengths; for example for the first cell $\frac{l_{reactor}}{U_b} \times \frac{U_b}{d} = \frac{l_{reactor}}{d} = L_{reactor}$.

Table 8. Table of Unit Cell RTD Moments for Various *Re*, *Pe*, $\bar{\delta}$, L_s and L_b = 1.1 from the Numerical Simulation

$\bar{\delta} = 3.11 \times 10^{-4}$	*Re*	4.5×10^{-5}					3
	Pe	10^5	10^4	10^3	10^2	10	10^5
L_s	$\bar{\tau}$			469			
0.25	$\bar{\mu}_1$ ($\times 10^{-2}$)	4.69	4.67	4.68	4.68	2.54	4.69
	$\bar{\mu}_2$ ($\times 10^{-5}$)	6.86	4.52	4.34	4.33	1.28	6.87
	$\bar{\sigma}^2$ ($\times 10^{-5}$)	4.66	2.33	2.15	2.14	0.63	4.67
	$\bar{\mu}_3$ ($\times 10^{-7}$)	162	64	59	59	10	163
	$\bar{\tau}$			1071			
1.00	$\bar{\mu}_1$ ($\times 10^{-2}$)	10.7	10.6	10.6	9.94	2.59	10.7
	$\bar{\mu}_2$ ($\times 10^{-5}$)	35.4	23.0	22.2	19.4	1.31	35.4
	$\bar{\sigma}^2$ ($\times 10^{-5}$)	24.0	11.7	10.9	9.51	0.644	24.0
	$\bar{\mu}_3$ ($\times 10^{-8}$)	183	71.7	66.9	55.6	0.984	183
	$\bar{\tau}$			3480			
4.00	$\bar{\mu}_1$ ($\times 10^{-3}$)	3.46	3.47	3.47	3.22	0.87	3.5
	$\bar{\mu}_2$ ($\times 10^{-5}$)	291	244	240	203	15	293
	$\bar{\sigma}^2$ ($\times 10^{-5}$)	171	123	120	100	7.14	173
	$\bar{\mu}_3$ ($\times 10^{-9}$)	360	255	246	187	3.68	368
	Re	4.5×10^{-5}					30
$\bar{\delta} = 10^{-3}$	*Pe*	10^5	10^4	10^3	10^2	10	10^5
L_s	$\bar{\tau}$			146			
0.25	$\bar{\mu}_1$ ($\times 10^{-2}$)	1.46	1.46	1.46	1.46	0.928	1.46
	$\bar{\mu}_2$ ($\times 10^{-4}$)	12.0	4.89	4.19	4.19	1.69	12.0
	$\bar{\sigma}^2$ ($\times 10^{-4}$)	9.91	2.76	2.07	2.05	0.83	9.91
	$\bar{\mu}_3$ ($\times 10^{-7}$)	18.6	2.49	1.77	1.79	0.463	18.5
	$\bar{\tau}$			333			
1.00	$\bar{\mu}_1$ ($\times 10^{-2}$)	3.32	3.33	3.33	3.33	2.08	3.33
	$\bar{\mu}_2$ ($\times 10^{-5}$)	6.22	2.52	2.22	2.19	0.856	6.19
	$\bar{\sigma}^2$ ($\times 10^{-5}$)	5.12	1.41	1.11	1.08	0.42	5.09
	$\bar{\mu}_3$ ($\times 10^{-7}$)	205	28.4	21.9	21.4	5.23	203
	$\bar{\tau}$			1083			
4.00	$\bar{\mu}_1$ ($\times 10^{-2}$)	10.8	10.8	10.8	10.7	7.06	10.8
	$\bar{\mu}_2$ ($\times 10^{-5}$)	40.4	24.5	23.3	22.9	9.64	40.7
	$\bar{\sigma}^2$ ($\times 10^{-5}$)	28.7	12.8	11.6	11.3	4.67	29.0
	$\bar{\mu}_3$ ($\times 10^{-8}$)	239	82.2	74.6	72.7	19.7	239
	Re	4.5×10^{-5}					300
$\bar{\delta} = 10^{-2}$	*Pe*	10^5	10^4	10^3	10^2	10	10^5
L_s	$\bar{\tau}$			15.3			
0.25	$\bar{\mu}_1$ ($\times 10^{-1}$)	1.55	1.56	1.55	1.56	1.35	1.55
	$\bar{\mu}_2$ ($\times 10^{-3}$)	9.75	1.37	0.516	0.437	0.325	9.75
	$\bar{\sigma}^2$ ($\times 10^{-3}$)	9.51	1.13	0.274	0.195	0.144	9.65
	$\bar{\mu}_3$ ($\times 10^{-5}$)	141	2.39	0.294	0.201	0.116	147
	$\bar{\tau}$			34			
1.00	$\bar{\mu}_1$ ($\times 10^{-1}$)	3.47	3.45	3.45	3.45	3.45	3.47
	$\bar{\mu}_2$ ($\times 10^{-3}$)	48.5	6.61	2.54	2.54	2.25	48.5
	$\bar{\sigma}^2$ ($\times 10^{-3}$)	47.3	5.42	1.35	1.35	1.06	47.5
	$\bar{\mu}_3$ ($\times 10^{-5}$)	1487	27.0	2.93	2.93	2.33	1490
	$\bar{\tau}$			110			
4.00	$\bar{\mu}_1$ ($\times 10^{-2}$)	1.10	1.10	1.10	1.10	1.01	1.10
	$\bar{\mu}_2$ ($\times 10^{-4}$)	21.8	3.89	2.45	2.25	1.71	22.7
	$\bar{\sigma}^2$ ($\times 10^{-4}$)	20.6	2.67	1.24	1.04	0.688	21.5
	$\bar{\mu}_3$ ($\times 10^{-6}$)	824	22.1	8.20	6.88	4.24	909

(2) A rapid rise in output concentration as the film exits the unit cell. The level of the first plateau reached is affected by the amount of tracer diffusing from the film to the vortex region.

(3) A slower rise in concentration with a number of plateaus. The length of each plateau corresponds to the time of a single circulation of the vortex in the slug. During this stage the concentration of the tracer in the outer parts of the vortex increases rapidly and approaches the film concentration. The inner parts of the vortex remain virtually tracer free.

(4) A very slow exponential increase to the final unit concentration value. This is typical behavior of the diffusion dominated process by which the tracer concentration in the inner part of the vortex slowly builds up.

The spline fitted $F(\bar{t})$ curves (see section "Residence-time distribution of unit cell") are differentiated to accurately obtain $E(\bar{t})$, which reveals some of the features more clearly. The plateaus in the $F(\bar{t})$ curve correspond to zero/very low-probability of an entering solute to remain in the system for the corresponding residence time. The peaks in the $E(\bar{t})$ curve correspond to the sharp rises in $F(\bar{t})$, and represent the outlet response of the unit cell to a single pulse input. It is worth noting that the area under the first peak in

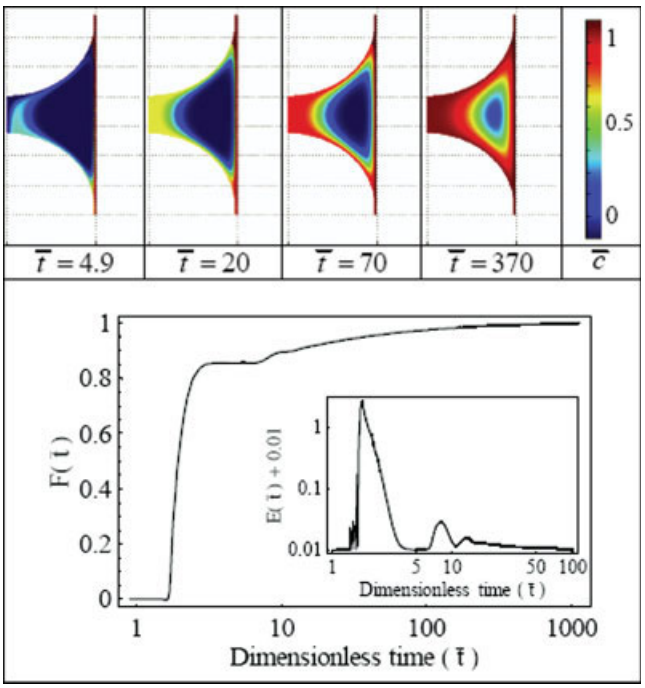

Figure 4. Variation with time of dimensionless unit cell concentration contours, density and residence-time distribution functions typical of high *Pe*.

($\bar{\delta} = 10^{-2}$, $Pe = 10^5$, $L_s = 0.25$, $Re = 4.5 \times 10^{-5}$). [Color figure can be viewed in the online issue, which is available at www.interscience.wiley.com.]

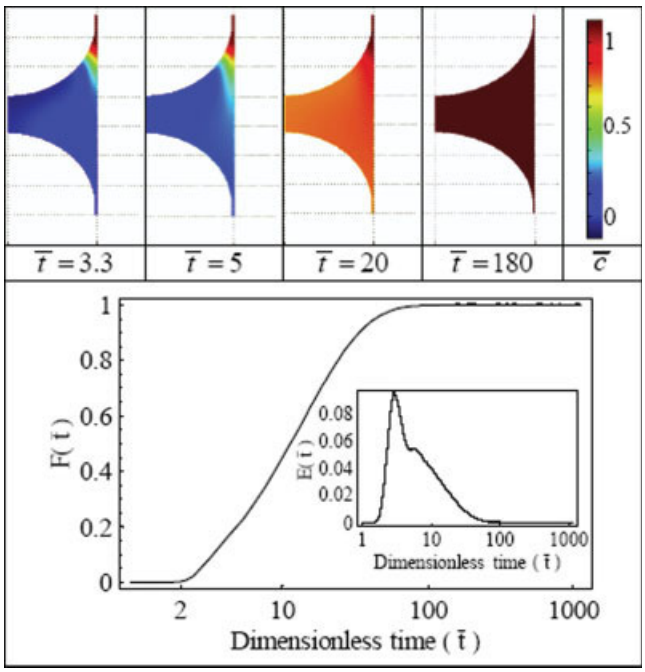

Figure 5. Variation with time of dimensionless unit cell concentration contours, density and residence-time distribution functions typical of low *Pe*.

($\bar{\delta} = 10^{-2}$, $Pe = 100$, $L_s = 0.25$, $Re = 4.5 \times 10^{-5}$). [Color figure can be viewed in the online issue, which is available at www.interscience.wiley.com.]

the $E(\bar{t})$ curve of Figure 4 represents the fraction of tracer which moves straight through the cell without interacting with the vortex.

The second concentration behavioral pattern appears in the cases of low-Peclet numbers {10, 100}, and is exemplified by Figure 5. Typical features of these curves are:

(1) An initial delay, corresponding to the time for the film to travel across the unit cell. There is no distinct film region observed from the concentration diagrams.

(2) The concentration in the unit cell rises rapidly to the final unit concentration value because of strong diffusivity. The region inside the slug is well mixed, and the exit concentration behavior will be shown to be reasonably approximated by an ideal continuous stirred tank (see section "CSTR-PFR combination").

The residence-time distribution curves of such systems were again obtained by interpolation and differentiation, and typically show no peaks corresponding to recirculation times (Figure 5).

To investigate the effect of *Re*, a film thickness $\bar{\delta} = 10^{-2}$ corresponding to $Ca \sim 10^{-3}$ was chosen as this has the largest *Re* range (Table 2). In addition the highest *Pe* for that film thickness $\bar{\delta}$ was used so that convection effects are most significant. The range was limited to $Pe = 10^5$ due to numerical artifacts. Table 8 shows almost identical values for all the moments for $Pe = 10^5$, and both *Re* extremes (4.5×10^{-5} and 300) representative of the near identical $E(t)$ curves obtained. It is, therefore, concluded that the Reynolds number has minimal effect on the residence-time distribution for the range of parameters studied.

Effect of Film Thickness $\bar{\delta}$ and Pe on Unit Cell RTD. With increasing film thickness, the peaks of the $E(\bar{t})$ curve become larger and more distinct (Figure 6). Similar behavior can be seen with increasing *Pe* (compare Figures 4 and 5). For $Pe = 10^2$ the peaks are no longer distinguishable. In Figure 6, the first peak grows with $\bar{\delta}$ as more tracer is able to move straight through without interacting with the vortex. When the film is thin or diffusion is more dominant (*Pe* small), it loses (by percentage) more of its tracer content by diffusion to the recirculating vortex as it moves through the slug, which implies that more of its contents mix with

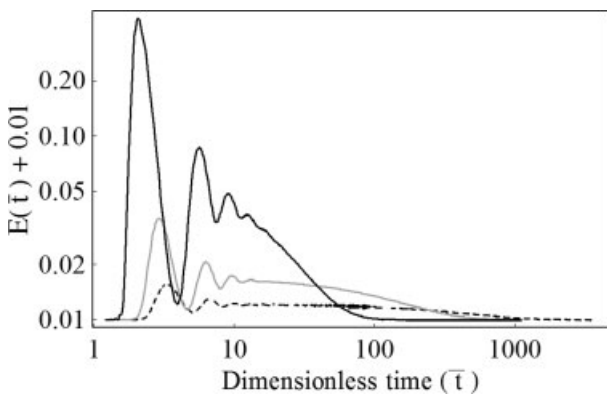

Figure 6. RTD curves of a unit cell for various film thicknesses $\bar{\delta}$, {Black: $\bar{\delta} = 10^{-2}$, Gray: $\bar{\delta} = 10^{-3}$, Dashed: $\bar{\delta} = 3.06 \times 10^{-4}$}. L_s = 0.25, *Pe* = 1,000, *Re* = 4.5×10^{-5}.

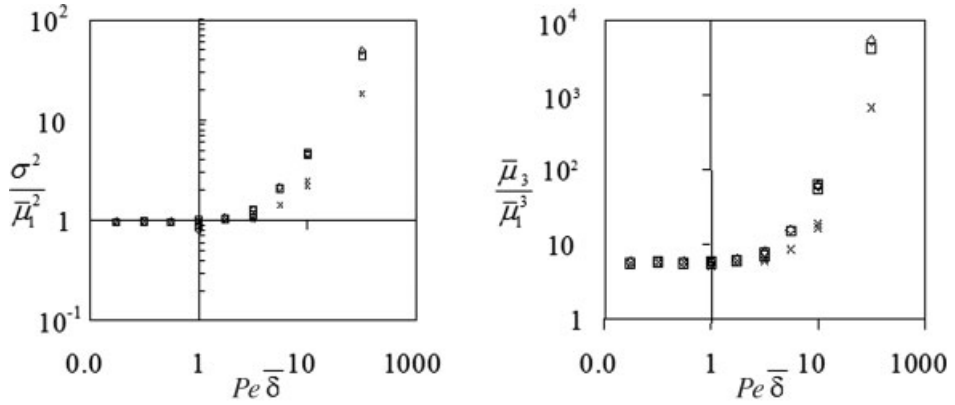

Figure 7. Effects of varying $Pe\bar{\delta}$, and the slug length on the shape of the RTD curve {Diamond: L_s = 0.25, Square: L_s = 1, Cross: L_s = 4}. Re = 4.5 × 10^{-5}.

the vortex. This effect is expected to increase with slug length, see section "Effect of L_s on unit cell RTD" following.

Since the unit cell RTD variation with Pe and $\bar{\delta}$ is attributed to the mass transfer between the film and the vortex, a pertinent dimensionless parameter for the characterization of mass transfer from the film is $Pe\bar{\delta}$. In Figure 7a and b normalized moments are presented as a function of $Pe\bar{\delta}$. The reason for the normalization (by dividing by the first moment raised to the appropriate power) is that the RTD of unit cells with different space-times can be compared directly. It is worth noting that there are some sets of different Pe and $\bar{\delta}$, which give rise to the same value of $Pe\bar{\delta}$ (Table 8).

It is observed that at $Pe\bar{\delta} < 10$ the normalized standard deviation and third moments are independent of $Pe\bar{\delta}$ and L_s. This indicates a CSTR-like RTD behavior. However, it should be noted that the spatial mixing behavior inside the slug depends on the Pe as can be seen by comparing Figures 4 and 5. For $Pe\bar{\delta} > 10$, the normalized moments increase with increasing $Pe\bar{\delta}$ and decreasing L_s.

Effect of L_s on Unit Cell RTD. Increasing the slug length increases accordingly the delay before the response in the outlet appears as the tracer has to travel through a longer film. The separation between the peaks on the RTD curve also increases as the resulting circulation time within a slug increases. The increased film length also means that there is a longer distance for diffusion to occur, and, hence, a larger proportion of the material carried in the film is transferred to the vortex region. This results in a decrease in the size of the peaks (Figure 8). Table 8 shows a trend of increasing standard deviation $\bar{\sigma}^2$ with increasing L_s.

For low Pe, where well mixed conditions in the slug are observed, the standard deviation is a monotonic function of space time (see Eq. 15). For high Pe, $\bar{\sigma}^2$ depends on the separation of the peaks, which is proportional to the vortex cycle time (see section "The model of Thulasidas et al."). The cycle time, in turn, increases with slug length. Note that the opposite trend is observed in Figure 7a due to the fact that the standard deviation is normalized.

Comparison to literature unit cell models

In this section, residence-time distribution curves and their moments produced by existing literature models are compared with the results of the current simulation.

CSTR-PFR Combination. The RTD curve of a unit cell approximated by a CSTR-PFR combination, where the CSTR corresponds to the slug, and the PFR to the film surrounding the bubble is[20]

$$E_{CSTR-PFR}(\bar{t}) = \begin{cases} \dfrac{e^{\frac{(L_b-1+2\bar{\delta})-\bar{t}}{\bar{t}_s}}}{\bar{t}_s} & \bar{t} \geq (L_b - 1 + 2\bar{\delta}) \\ 0 & \bar{t} < (L_b - 1 + 2\bar{\delta}) \end{cases} \quad (13)$$

The first three moments are calculated as follows

$$\bar{\mu}_1 = \bar{t}_s + (L_b - 1 + 2\bar{\delta}) \quad (14)$$

$$\bar{\mu}_2 = (L_b - 1 + 2\bar{\delta})^2 + 2(L_b - 1 + 2\bar{\delta})\bar{t}_s + 2\bar{t}_s^2 \quad (15)$$

$$\bar{\mu}_3 = (L_b - 1 + 2\bar{\delta})^3 + 3(L_b - 1 + 2\bar{\delta})^2\bar{t}_s + 6(L_b - 1 + 2\bar{\delta})\bar{t}_s + 6\bar{t}_s^3 \quad (16)$$

where $\bar{t}_s$ is the dimensionless space-time of the slug, which can be calculated from the slug geometry

$$\bar{t}_s = \frac{V}{A_f d} = \frac{\bar{R}^2(2(\bar{R} - \bar{\delta}) + L_s) - \frac{4}{3}(\bar{R} - \bar{\delta})^3}{2\bar{R}(\bar{R}^2 - (\bar{R} - \bar{\delta})^2)} \quad (17)$$

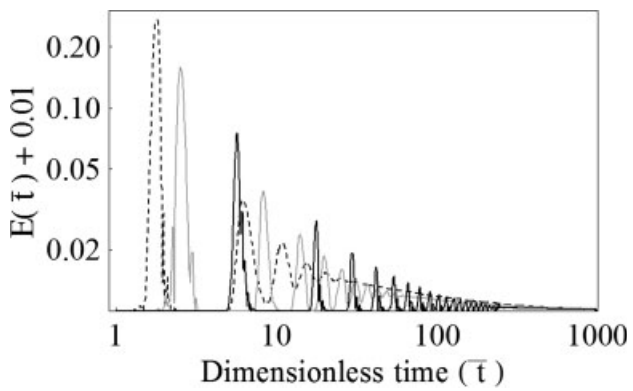

Figure 8. RTD curves of a unit cell for various slug lengths L_s {Dashed: L_s = 0.25, Gray: L_s = 1, Black: L_s = 4}. Pe = 10^5, $\bar{\delta}$ = 3.04 × 10^{-4}, Re = 4.5 × 10^{-5}.

This model has no fitting parameters and, can, thus, be easily used. For a film of zero length ($L_b = 1-2\bar{\delta}$), the CSTR-PFR reduces to a CSTR with $\bar{\mu}_1 = \bar{t}_s$, $\mu_2 = 2\bar{t}_s^2$ and $\bar{\mu}_3 = 6\bar{t}_s^3$, which when normalized give $\overline{\mu}_3/\overline{\mu}_1^3 = 6$, $\overline{\sigma}^2/\overline{\mu}_1^2 = 1$. These values are the same as those found at the limit of small $Pe\bar{\delta}$, and small L_b ($L_b = 1.1 - 2\bar{\delta}$), as can be seen from Figure 7a and 7b. Qualitatively, however, it is quite clear that the single exponential decay in the residence-time distribution is not going to be able to account for the multipeak behavior observed in the residence-time distribution curves of high Peclet numbers. Although it contains terms relating to film thickness and slug length, the Peclet number does not feature in the equation, and the difference between high- and low-Peclet number cases cannot be resolved.

An example where this model is a good representation of the numerical results is shown in Figure 9. It is worth noting the logarithmic time scales used, and that the models agree reasonably well for $\bar{t} > 10$. By comparing the various moments of the CSTR-PFR model with the CFD model in Table 10, it can be observed that the CSTR-PFR model agrees best with the CFD model at intermediate Pe. At higher Pe the model is not a good representation of the unit cell due to the lower contribution of diffusion to mixing. At lower Pe values, discrepancies are due to the reduced contribution of convection to mixing.

Two-Region Model. This model differs from the previous CSTR-PFR model in that the slug is split into two regions (film and vortex), where each is modelled as a CSTR, and a mass-transfer coefficient accounts for the mass transfer between the two as proposed by Pedersen and Hovarth.[21] The output concentration of this model is given by

$$E_{2Region}(\bar{t}) = \begin{cases} -\dfrac{e^{-\frac{1}{2}(\zeta+\eta+\theta+\kappa)((\bar{t}-(L_b-1+2\bar{\delta}))}(-\zeta-\eta+\theta+\kappa)(\zeta+\eta+\theta+\kappa))}{4\zeta} & \\ & \bar{t} \geq (L_b-1+2\bar{\delta}) \\ -\dfrac{e^{[\zeta-\frac{1}{2}(\zeta+\eta+\theta+\kappa)](\bar{t}-(L_b-1+2\bar{\delta}))}(\zeta-\eta+\theta+\kappa)\left[\zeta-\frac{1}{2}(\zeta+\eta+\theta+\kappa)\right]}{2\zeta} & \\ 0 & \bar{t} < (L_b-1-2\bar{\delta}) \end{cases} \tag{18}$$

The first three moments of the two-region model can be easily calculated as

$$\bar{\mu}_1 = \frac{(\theta+\kappa)}{\eta\kappa} + (L_b-1+2\bar{\delta}) \tag{19}$$

$$\bar{\mu}_2 = \frac{2\theta\,(\eta+\theta) + 2(2+(L_b-1+2\bar{\delta})\eta)\theta\kappa}{\eta^2\kappa^2} + \frac{(2+(L_b-1+2\bar{\delta})\eta(2+(L_b-1+2\bar{\delta})\eta))\kappa^2}{\eta^2\kappa^2} \tag{20}$$

$$\bar{\mu}_3 = \frac{6\theta(\eta+\theta)^2 + 6\theta(3\theta+\eta(2+(L_b-1+2\bar{\delta})(\eta+\theta)))\kappa}{\eta^3\kappa^3} + \frac{3(6+(L_b-1+2\bar{\delta})\eta(4+(L_b-1+2\bar{\delta})\eta))\theta\kappa^2}{\eta^3\kappa^3} + \frac{(6+(L_b-1+2\bar{\delta})\eta(6+(L_b-1+2\bar{\delta})\eta(3+(L_b-1+2\bar{\delta})\eta)))\kappa^3}{\eta^3\kappa^3} \tag{21}$$

where

$$\eta = \frac{A_f d}{V_1} \tag{22}$$

$$\theta = \frac{Sh}{Pe}\frac{A_s d}{V_1} \tag{23}$$

$$\kappa = \frac{Sh}{Pe}\frac{A_s d}{V_2} \tag{24}$$

$$\zeta = \sqrt{(\eta+\theta+\kappa)^2 - 4\eta\kappa} \tag{25}$$

It is difficult to calculate the exact volumes of the film and the vortex region, V_1 and V_2, respectively, and transfer area between them, A_s, without identifying the streamline separating the two regions. They can, however, be estimated reasonably well by assuming the thickness of the film region in the slug to be equal to the film thickness surrounding the bubble

$$V_1 = \pi\bar{R}^2(\bar{L}_s + 2(\bar{R}-\bar{\delta}))\left(\frac{\bar{R}^2}{(\bar{R}-\bar{\delta})^2} - 1\right) \tag{26}$$

$$V_2 = \left[\pi\bar{R}^2(L_s + 2(\bar{R}-\bar{\delta})) - \frac{4}{3}\pi(\bar{R}-\bar{\delta})^3\right] - V_1 \tag{27}$$

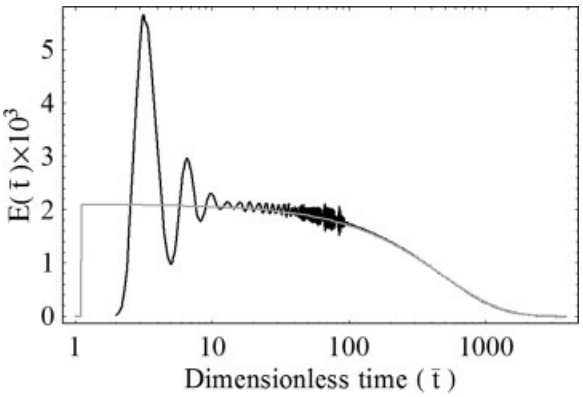

Figure 9. RTD of unit cell for two models {Black: CFD Simulation, Gray: CSTR-PFR} for the case of {$\bar{\delta}$ = 3.06 × 10^{-4}, *Pe* = 1,000, *Re* = 4.5 × 10^{-5}, L_s = 0.25, L_b = 1.1 − 2$\bar{\delta}$}.

$$A_s = 2\pi(\bar{R} - \bar{\delta})(L_s + 2(\bar{R} - \bar{\delta})) \tag{28}$$

This model has a single fitting parameter, the Sherwood number $Sh = (k_L d)/D$, and includes in its formulation all the dimensionless parameters affecting the behavior of the slug. Published values for *Sh* are usually obtained from experiments on liquid to wall mass transfer.[5,6,8,22,23] Rather than relying on such values, however, the model was fitted to the curves obtained from the CFD simulation in this work using *Sh* as the fitting parameter. The method of least-square error (see Eq. 6) was used to fit *Sh,* and then the 2nd and 3rd moments were compared. Fitted *Sh* numbers can be found in Table 9.

The calculated *Sh* values for the two-region model were found to be smaller by less than a factor of two than those predicted by Kreutzer's correlation,[8] and by up to a factor of four than those predicted by the correlation of Gruber and Melin.[23] It should be noted that the latter correlation is a fit over a very large range of slug length values ($1 \leq L_s \leq 600$). The values considered here are very much towards the lower end of that range, which may explain the larger discrepancies. Furthermore, the discrepancy may also be due to the fact that the above researchers calculated the *Sh* for mass transfer between the slug and the wall, while in this work the Sherwood is for mass transfer between the two regions of the slug. This difference, however, is not expected to be significant due to the small film thickness.

The correlation of Kreutzer[8] relates the *Sh* to the ratio $L_{reactor}/Pe$ and L_s. For the cases analyzed here, $0.2 < L_{reactor}/Pe \leq 2$, which places them at the range where *Sh* is insensitive to small changes in the ratio (Figure 10), which can also be seen in Table 9. The trend of increasing *Sh* with decreasing L_s, seen in Figure 10, is not always observed for the CFD model.

A typical RTD curve at high-Peclet numbers is shown in Figure 11. Qualitatively it is not surprising that the exponential sum expression, which results from the two-region model cannot account for the shapes of residence time curves obtained. It is also not surprising that for $Pe\bar{\delta} > 10$ the first three moments match those of the numerical model slightly better than those of the CSTR-PFR model (Table 10), which does not have an adjustable parameter.

Interestingly, at $Pe\bar{\delta} < 10$ an optimum *Sh* could not be found, but the fitting was improved when *Sh* was increased to very large values. The residual error plateaued to a constant value, and was then insensitive to further increases in *Sh,* which were about two or more orders of magnitude larger than those predicted from correlations.[8] The limit at large *Sh* for the two-region model is the CSTR-PFR model, from which it can be clearly concluded that the two-region model offers no advantage over the CSTR-PFR one for $Pe\bar{\delta} < 10$.

The Model of Thulasidas et al. In contrast to the earlier models, the model by Thulasidas et al.[1] takes into account the cyclic nature of the output, which results from a combination of dominating axial convection and slow radial diffusion. Certain points of the model development are repeated here to provide insight into the output given by the model. The model assumes a constant output concentration from the unit cell for the duration of a cycle (the time for a complete rotation of a vortex in the slug). To explain how this assumption arises consider that the concentration is determined from the interaction of the film with the vortex which lasts for the entire cycle. During that cycle the vortex region interacts with a length of the film approximately double the slug length. The vortex material which interacts with the film in the first half cycle moves near the centerline of the tube in the second half cycle, and is assumed not to interact with the other part of the vortex (now interacting with the film). This results in the film experiencing the same conditions as it moves through the unit cell for the duration of one cycle, which results in a constant output.

Neglecting the velocity gradients in the liquid slug, and assuming constant initial concentrations in the slug and the film, a unidirectional diffusion equation along the cross section is solved for time equal to one half cycle. The concentrations in the film and the coflowing part of the vortex are averaged. The averaged concentration of the film at the end of the half cycle is the output concentration for the duration of the cycle, while that of the top half vortex is the average concentration of the vortex after a complete cycle. The model is then repeated starting with the averaged concentration of the vortex and the "new" inflow concentration of the film, which is the output of the upstream unit cell.

The averaged concentrations obtained from the model, with the typographical errors in the expressions corrected from the original,[1] were nondimensionalized, and are given for the film in Eq. 29 and for the vortex region of the slug in Eq. 30

Table 9. Calculated Sherwood Numbers for the Two-Region Model

Sh												
$\bar{\delta} = 3.04 \times 10^{-4}$				$\bar{\delta} = 10^{-3}$				$\bar{\delta} = 10^{-2}$			
Pe	10^3	10^4	10^5	*Pe*	10^3	10^4	10^5	*Pe*	10^3	10^4	10^5
L_s				L_s				L_s			
0.25	∞	60	65	0.25	∞	65	86	0.25	193	56	63
1.0	∞	37	37	1.0	197	39	47	1.0	98	41	41
4.0	∞	39	31	4.0	∞	40	35	4.0	230	39	33

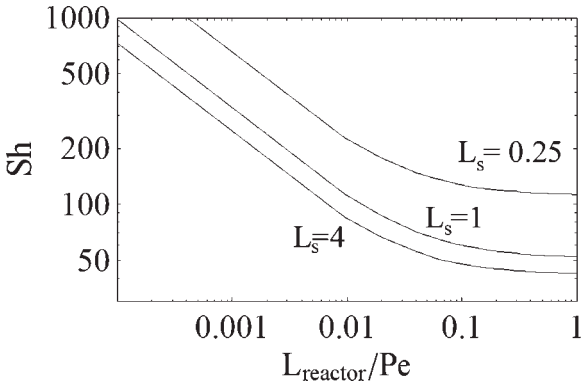

Figure 10. Variation of *Sh* with $L_{reactor}/Pe$ for various L_s, based on the correlation by Kreutzer.[8]

$$\bar{c}_{f,av} = 1 + 4[\bar{c}_{10} - \bar{c}_{20}]\bar{r}_1^2 + \sum_{n=1}^{\infty} e^{-\frac{\lambda_n^2 \bar{t}}{Pe}} \left[\frac{-16[\bar{c}_{10} - \bar{c}_{20}]\bar{r}_1^2 J_1^2(\lambda_n \bar{r}_1)}{\left((\frac{1}{2})^2 - \bar{r}_1^2\right)\lambda_n^2 J_0^2(0.5\lambda_n)} \right] \quad (29)$$

$$\bar{c}_{v,av} = 1 + 4[\bar{c}_{10} - \bar{c}_{20}]\bar{r}_1 + \sum_{n=1}^{\infty} e^{-\frac{\lambda_n^2 \bar{t}}{Pe}} \left[\frac{16[\bar{c}_{10} - \bar{c}_{20}]\bar{r}_1 J_1(\lambda_n \bar{r}_1)[\bar{r}_1 J_1(\lambda_n \bar{r}_1) - \bar{r}_0 J_1(\lambda_n \bar{r}_0)]}{(\bar{r}_1^2 - \bar{r}_0^2)\lambda_n^2 J_0^2(\frac{\lambda_n}{2})} \right] \quad (30)$$

where

$$\bar{r}_1 = \frac{1}{2}\sqrt{2 - \psi} \quad (31)$$

$$\bar{r}_0 = \frac{1}{2}\frac{\sqrt{2 - \psi}}{\sqrt{2}} \quad (32)$$

obtained from Thulasidas et al.,[2] and nondimensionalized using the radius. The eigenvalues are given in terms of the zeros of the Bessel function of the first-order

$$\lambda_n = 2\, Z_{1n} \quad (33)$$

The average film concentration is evaluated using Eq. 29 after a time equal to *half* a cycle time of the vortex with initial concentrations $\bar{c}_{10}$, the initial average vortex concentration, and $\bar{c}_{20} = 1$, the initial film concentration at the beginning of each cycle always taken as 1 for the step-tracer input. This value is used as the output for the total cycle time. Similarly, the average vortex concentration is evaluated using Eq. 30. The procedure is repeated using the previous averaged vortex concentration for a new $\bar{c}_{10}$, and the constant value of 1 for $\bar{c}_{20}$. The cycle time can be calculated from expression 34, which has been modified from the expression given by Thulasidas et al. to account for the liquid volume around the bubble caps. $\bar{\tau}_{cycle}$ is calculated by using a length obtained by approximating the vortex volume to a cylinder, and the area averaged velocity in either of the vortex flow directions.

$$\bar{\tau}_{cycle} = \frac{2 + 6\, L_s + 4\bar{\delta}(3 + 4\bar{\delta}(2\bar{\delta} - 3))}{3(1 + 8(\bar{\delta} - 1)\bar{\delta})} \quad (34)$$

The density function $F(\bar{t})$ obtained by the Thulasidas et al. model is a series of plateaus, such as those seen with the current model at high *Pe* (Figure 4). The corresponding residence-time distribution $E(\bar{t})$ from Thulasidas' model is a series of ideal pulses at times corresponding to the vortex circulation times.

The model of Thulasidas et al. was implemented using the first hundred terms of the series, and the moments are given in Table 10. It can be seen, by comparing the second and third moments, that it performs worst at the extremes of high-and low-Peclet numbers. The way the model is formulated is not conservative, so material which crosses the centre of the vortex is neglected in the averaging. This explains why the difference between the moments of the Thulasidas et al. model and those of the numerical calculations are worst at low *Pe*. In addition the first moments do not match even at high *Pe*. This is attributed to inaccurate estimation of the cycle time. $\bar{\tau}_{cycle}$ is the only parameter where the slug length features; from expression 34, a longer cycle time translates to a longer slug, and, hence, corresponds to larger space-times. Sensitivity analysis on $\bar{\tau}_{cycle}$ showed a small change of the variable to have a significant effect on the first moment. If the suggested expression of the cycle time by Thulasidas et al. is used instead of Eq. 34, the performance is much worse. Also the first moments of the Thulasidas et al. model are closer to the numerical ones with increasing slug length as the regions near the caps, neglected in the Thulasidas model, have lower contribution to the circulation time, as compared to the rest of the unit cell. Order of magnitude analysis of the generated moments, using the cycle time given by expression 34, shows a worsening performance when changing from $Pe = 10^4$ to $Pe = 10^5$, which may be attributed to the averaging of concentration carried out at the end of each half cycle time.

Reactor RTD Curves, Comparison with Literature Experimental Results. To demonstrate how the results obtained from the CFD model developed here are used to calculate the reactor residence-time distribution, a specific example is

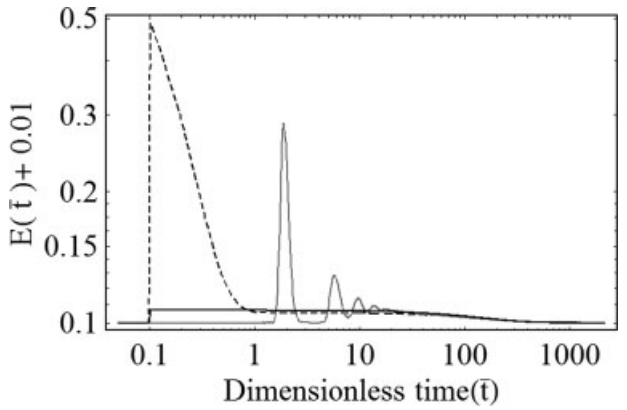

Figure 11. RTD of a unit cell for different models {Gray: Numerical simulation, Dashed: Two region, Black: CSTR-PFR} for the case of {$\bar{\delta} = 10^{-3}$, $Re = 4.5 \times 10^{-5}$, $L_s = 0.25$, $L_b = 1.1 - 2\bar{\delta}$, $Pe = 10^4$}.

The best fitting Sherwood number for the two-region model was found to be *Sh* = 65.

Table 10. Table of Unit Cell Moments as Calculated from the RTD of Various Models

$\bar{\delta} = 3.11 \times 10^{-4}$		CSTR-PFR	CFD	Two-Region	Thulasidas et al.	CFD	Two-Region	Thulasidas et al.	CFD	Two-Region	Thulasidas et al.	CFD	Two-Region	Thulasidas et al.
L_s			$Pe = 10^5$			$Pe = 10^4$			$Pe = 10^3$			$Pe = 10^2$		
0.25	$\bar{\mu}_1$ ($\times 10^{-2}$)	4.69	4.69	4.69	5.12	4.67	4.69	5.12	4.68	4.69	5.12	4.68	4.69	5.98
	$\bar{\mu}_2$ ($\times 10^{-5}$)	4.40	6.86	6.07	5.19	4.52	4.58	5.30	4.34	4.40	5.22	4.33	4.40	7.09
	$\bar{\sigma}^2$ ($\times 10^{-5}$)	2.20	4.66	3.87	2.57	2.33	2.38	2.68	2.15	2.20	2.60	2.14	2.20	3.51
	$\bar{\mu}_3$ ($\times 10^{-8}$)	6.19	16.2	11.8	9.75	6.42	6.71	8.23	5.94	6.19	8.01	5.93	6.19	12.5
1.0	$\bar{\mu}_1$ ($\times 10^{-2}$)	10.7	10.7	10.7	11.2	10.6	10.7	11.2	10.6	10.7	11.2	9.94	10.7	16.0
	$\bar{\mu}_2$ ($\times 10^{-5}$)	22.9	35.4	32.6	25.2	23.0	23.9	25.0	22.2	22.9	24.9	19.4	22.9	50.6
	$\bar{\sigma}^2$ ($\times 10^{-5}$)	11.5	24.0	21.1	12.7	11.7	12.4	12.5	10.9	11.5	12.4	9.51	11.5	25.1
	$\bar{\mu}_3$ ($\times 10^{-7}$)	737	1830	1490	951	717	800	824	66.9	73.7	818	55.6	73.7	2378
4.0	$\bar{\mu}_1$ ($\times 10^{-2}$)	34.8	34.6	34.8	35.4	34.7	34.8	35.4	34.7	34.8	39.2	32.2	34.8	64.6
	$\bar{\mu}_2$ ($\times 10^{-5}$)	242	291	281	255	244	247	250	240	242	305	203	242	766
	$\bar{\sigma}^2$ ($\times 10^{-5}$)	121	171	159	130	123	125	125	120	121	152	100	121	349
	$\bar{\mu}_3$ ($\times 10^{-9}$)	253	360	339	281	255	263	270	246	253	358	187	253	358
$\bar{\delta} = 10^{-3}$		CSTR-PFR	CFD	Two-Region	Thulasidas et al.	CFD	Two-Region	Thulasidas et al.	CFD	Two-Region	Thulasidas et al.	CFD	Two-Region	Thulasidas et al.
L_s			$Pe = 10^5$			$Pe = 10^4$			$Pe = 10^3$			$Pe = 10^2$		
0.25	$\bar{\mu}_1$ ($\times 10^{-2}$)	1.46	1.46	1.46	1.39	1.46	1.46	1.59	1.46	1.46	1.59	1.46	1.46	1.86
	$\bar{\mu}_2$ ($\times 10^{-5}$)	0.436	1.20	0.818	0.57	0.49	0.478	0.52	0.429	0.436	0.51	0.419	0.436	0.69
	$\bar{\sigma}^2$ ($\times 10^{-4}$)	2.13	9.91	6.05	3.21	2.76	2.65	2.67	2.07	2.13	2.57	2.05	2.13	3.41
	$\bar{\mu}_3$ ($\times 10^{-7}$)	1.87	18.6	6.89	4.17	2.49	2.35	2.87	1.77	1.87	2.43	1.79	1.87	3.90
1.0	$\bar{\mu}_1$ ($\times 10^{-2}$)	3.33	3.32	3.33	3.47	3.33	3.33	3.47	3.33	3.33	3.48	3.33	3.33	4.96
	$\bar{\mu}_2$ ($\times 10^{-5}$)	2.22	6.22	4.56	2.51	2.52	2.51	2.49	2.22	2.23	2.43	2.19	2.22	4.87
	$\bar{\sigma}^2$ ($\times 10^{-5}$)	1.11	5.12	3.45	1.31	1.41	1.39	1.29	1.11	1.12	1.21	1.08	1.11	2.41
	$\bar{\mu}_3$ ($\times 10^{-8}$)	2.22	20.5	9.39	3.65	2.84	2.82	2.74	2.19	2.23	2.60	2.14	2.22	7.02
4.0	$\bar{\mu}_1$ ($\times 10^{-2}$)	10.8	10.8	10.8	11.0	10.8	10.8	11.0	10.8	10.8	12.2	10.7	10.8	12.2
	$\bar{\mu}_2$ ($\times 10^{-5}$)	23.4	40.4	36.7	24.0	24.5	24.6	24.5	23.3	23.4	29.5	22.9	23.4	29.2
	$\bar{\sigma}^2$ ($\times 10^{-5}$)	11.7	28.7	25.01	11.9	12.8	12.9	12.4	11.6	11.7	14.7	11.3	11.7	14.3
	$\bar{\mu}_3$ ($\times 10^{-8}$)	76.1	239	187	99.1	82.2	83.9	83.4	74.6	76.1	108	72.7	76.1	111
$\bar{\delta} = 10^{-2}$		CSTR-PFR	CFD	Two-Region	Thulasidas et al.	CFD	Two-Region	Thulasidas et al.	CFD	Two-Region	Thulasidas et al.	CFD	Two-Region	Thulasidas et al.
L_s			$Pe = 10^5$			$Pe = 10^4$			$Pe = 10^3$			$Pe = 10^2$		
0.25	$\bar{\mu}_1$ ($\times 10^{-1}$)	1.53	1.55	1.53	1.69	1.56	1.53	1.69	1.55	1.52	1.70	1.56	1.53	2.02
	$\bar{\mu}_2$ ($\times 10^{-3}$)	0.466	9.75	5.53	3.47	1.37	1.03	1.14	0.516	0.483	0.622	0.437	0.470	0.739
	$\bar{\sigma}^2$ ($\times 10^{-3}$)	0.231	9.51	5.29	3.18	1.13	0.801	0.853	0.274	0.248	0.332	0.195	0.235	0.331
	$\bar{\mu}_3$ ($\times 10^{-5}$)	0.213	141	32.4	14.7	2.39	1.08	1.56	0.294	0.228	0.458	0.201	0.222	0.542
1.0	$\bar{\mu}_1$ ($\times 10^{-1}$)	3.43	3.47	3.43	3.64	3.45	3.43	3.66	3.45	3.43	3.69	3.45	3.42	7.21
	$\bar{\mu}_2$ ($\times 10^{-3}$)	2.34	48.5	28.0	10.8	6.61	4.90	3.96	2.54	2.45	2.67	2.25	2.35	9.67
	$\bar{\sigma}^2$ ($\times 10^{-3}$)	1.17	47.3	26.8	9.48	5.42	3.73	2.62	1.35	1.27	1.31	1.06	1.18	4.47
	$\bar{\mu}_3$ ($\times 10^{-5}$)	2.40	1487	362	65.8	27.0	10.7	8.69	2.93	2.62	3.89	2.33	2.49	23.6
4.0	$\bar{\mu}_1$ ($\times 10^{-1}$)	11.0	11.0	11.0	11.5	11.0	11.0	11.5	11.0	11.0	12.9	11.0	11.0	21.6
	$\bar{\mu}_2$ ($\times 10^{-4}$)	2.42	21.8	15.9	6.58	3.89	3.56	2.44	2.45	2.44	2.21	2.25	2.42	8.45
	$\bar{\sigma}^2$ ($\times 10^{-4}$)	1.21	20.6	14.7	5.26	2.67	2.35	1.10	1.24	1.23	0.55	1.04	1.21	3.78
	$\bar{\mu}_3$ ($\times 10^{-6}$)	7.97	824	357	62.5	22.1	17.4	15.5	8.2	8.10	13.7	6.88	8.0	64.1

Table 11. Parameters used in the Reactor RTD Calculations

Ca	2.84×10^{-4}
$\bar{\delta}$	2.89×10^{-3}
Pe	19,048
L_s	4.15
L_b	13
$L_{reactor}$	285

presented, utilizing the experimental data of Thulasidas et al.,[1] with the corresponding parameters given in Table 11. The residence-time distribution curve of a unit cell is given in Figure 12, and is typical of high Pe (see section "General features of the unit cell RTD/spatial concentration contours and the effect of the dimensionless parameters").

The concentration output of each unit cell exiting the reactor for a single unit cell pulse (Figure 2) is obtained from evaluating the inverse Laplace transform of the functions in Table 6 at dimensionless times given in Table 7, and the results are presented as a barchart in Figure 13. The figure shows that cell 1 exiting the reactor still has the majority of the tracer inside it with subsequent cells containing less and less material. From the velocity of each unit cell and its length, as well as the length of the reactor, the concentration at different times can be plotted and converted to the reactor residence-time distribution curve $E_{reactor}(\bar{t})$ when normalized (Figure 14). Given the experimental input signal $c_i(\bar{t})$ and the $E_{reactor}(t)$ curve, the dimensional version of $E_{reactor}(\bar{t})$, a convolution integral of the two curves allows the calculation of the reactor output curve (Figure 15). The results match the experimental results very well. It should be noted, however, that the model of Thulasidas et al.[1] also matched their results well, despite being the worst performer amongst the models considered here. The model proposed by Kreutzer also gives a reasonable match to the results, although not as good.[8] The reason for all models matching the results is probably the relative short length of the reactor considered. The distinction between all the models should become more apparent with increasing reactor length.

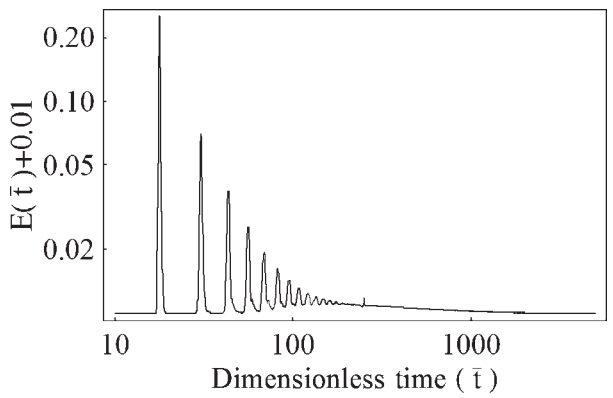

Figure 12. Residence-time distribution curve in a unit cell calculated from the current CFD model for the experimental data by Thulasidas et al.[1] when unit pulse is introduced in unit cell 1.

$\bar{\delta} = 2.89 \times 10^{-3}$, $Pe = 19{,}048$, $L_s = 4.15$, (see also Table 11 for the values of all parameters used).

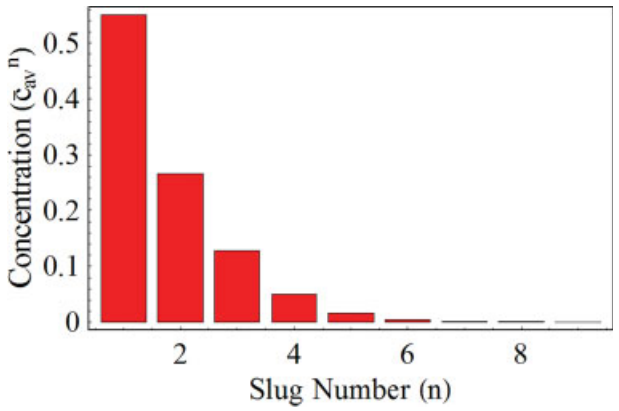

Figure 13. Average concentration of cells when exiting the reactor corresponding to Figure 12 for $\bar{\delta} = 2.89 \times 10^{-3}$, $Pe = 19{,}048$, $L_s = 4.15$, $L_{reactor} = 285$.

[Color figure can be viewed in the online issue, which is available at www.interscience.wiley.com.]

Conclusions

A numerical model based on CFD has been developed for the prediction of axial mixing during Taylor flow in microchannels. The response of a single unit cell (comprising of a liquid slug and two half bubbles) to a step-tracer input is analyzed, and its residence-time distribution evaluated. Since no assumptions were made for the flow and mixing within the liquid slug, the predictions of this model can be used to evaluate different literature methodologies for the calculation of axial mixing in Taylor flow systems.

Two trends were found for the residence-time distribution $E(\bar{t})$ of a single unit cell. At high Pe the $E(\bar{t})$ curve shows characteristic peaks at times corresponding to the vortex circulation times within the liquid slugs. The concentration patterns within the slugs follow the flow streamlines at least initially. At low Pe, the $E(\bar{t})$ curve shows a single peak that decays slowly with $\bar{t}$, while the concentration inside the liquid slug rises rapidly with $\bar{t}$ to its final value because of strong diffusion.

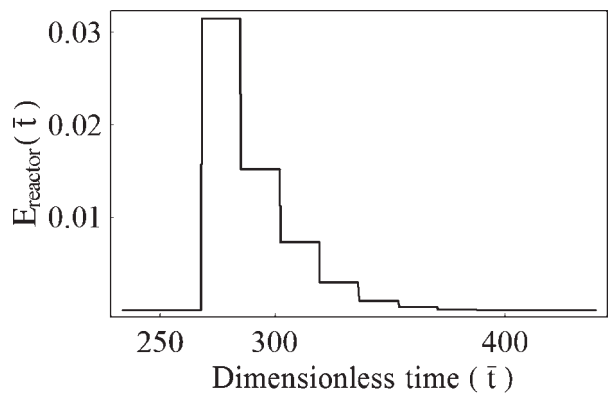

Figure 14. Residence-time distribution of the reactor corresponding to Figure 13 for $\bar{\delta} = 2.89 \times 10^{-3}$, $Pe = 19{,}048$, $L_s = 4.15$, $L_{reactor} = 285$.

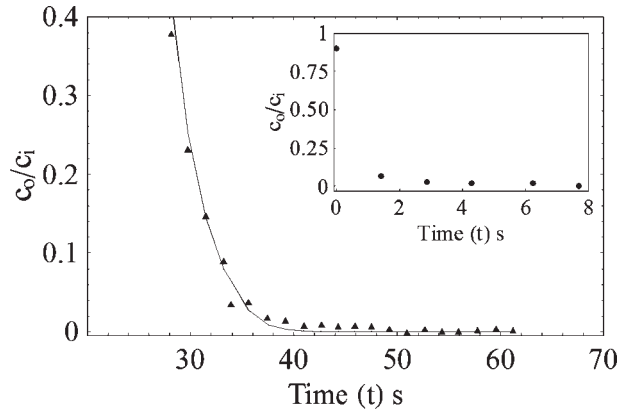

Figure 15. Experimental (points) and theoretical output (line), calculated from the current model, of a single Taylor-flow capillary reactor vs. time for $\bar{\delta}$ = 2.89 × 10^{-3}, *Pe* = 19,048, L_s = 4.15, $L_{reactor}$ = 285.

The top righthand corner insert shows the input tracer signal into the capillary as measured experimentally from Thulasidas et al.[1]

The earlier model was used to study the axial mixing in a unit cell for a large range of dimensionless parameters that cover reactor sizes and fluid properties encountered in microreactor applications. It was found that *Re* has negligible effect on the residence-time distribution curve. Increasing film thickness or *Pe* resulted in larger and more distinct peaks in the $E(\bar{t})$ curve. On the other hand, with increasing L_s, the separation between the peaks increases while their size decreases. The diffusion from film to vortex was found to depend on $Pe\bar{\delta}$. For $Pe\bar{\delta} \leq 10$ the normalized moments are independent of $Pe\bar{\delta}$ and L_s, similarly to CSTR RTD curves irrespective of spacial mixing pattern inside the liquid slug which depends on *Pe*. At high $Pe\bar{\delta}$ the normalized moments increase with $Pe\bar{\delta}$ at a rate dependent on L_s; higher L_s reduces the normalised moments associated with $Pe\bar{\delta}$.

Different literature models where then evaluated against the current CFD predictions. The first three moments of the residence time distribution curves were used for the comparisons. The following were found

(1) Of the models considered the CSTR-PFR matches the CFD results for $Pe\bar{\delta} < 10$. The predictions of the RTD curve moments when this model was used were best for medium *Pe* ($100 \leq Pe \leq 1000$).

(2) A fitted two-region model with *Sh* as a single fitting parameter, gives better agreement with the current CFD model than the CSTR-PFR model for $Pe\bar{\delta} > 10$. However, the fitted values of *Sh* are up to four times smaller than those found by literature correlations, and do not show correct trends with respect to increasing slug length.

(3) The method proposed by Thulasidas et al.[1] gave the least accurate predictions.

From the residence-time distribution curves of individual unit cells, the residence-time distribution of the whole reactor can be evaluated. Given a tracer input concentration, by means of a convolution method the concentration at the output of the reactor at different times can be found. The method was used for the experimental data by Thulasidas et al.,[1] and good agreement was found. It has to be noted, however, that the short length of the reactor used in these experiments did not allow proper differentiation between different models, and the other models also showed good agreement with the experimental data.

Acknowledgments

This work was supported by the EU KEMiCC project G1RD-CT2000-00469.

Notation

A_s = area separating the vortex and film regions in slug, m^2
A_f = cross sectional area of film, m^2
c = tracer concentration, kg m^{-3}
$C = \mathcal{L}(c)$, Laplace transform of c
Ca = capillary number, $\mu U_b/\gamma$
d = microchannel diameter, m
D = diffusivity of tracer species, m^2/s
$E(t)$ = unit cell residence-time distribution (RTD) curve, s^{-1}
$E(\bar{t})$ = dimensionless $E(t)$, $dU_bE(t)$
$E_{CSTR\text{-}PFR}(\bar{t})$ = dimensionless CSTR-PFR model RTD curve
$E_{reactor}(\bar{t})$ = dimensionless reactor RTD curve
$E_{2Region}(\bar{t})$ = dimensionless two-region model RTD curve
$E(\bar{s}) = \mathcal{L}(E(\bar{t}))$, Laplace transform of $E(\bar{t})$
$F(\bar{t})$ = dimensionless density function
$F_{model}(\bar{t})$ = dimensionless density function from fitted model
$F(\bar{s}) = \mathcal{L}(F(\bar{t}))$, Laplace transform of $F(\bar{t})$
Fr = Froude number, U_b^2/gd
g = acceleration due to gravity, m/s^2
J_0, J_1 = Bessel functions of the first kind of order zero and one
k_L = mass-transfer coefficient between film and vortex, ms^{-1}
$\mathcal{L}$ = Laplace transform operator
l_b = Taylor bubble length, m
l_{cell} = unit cell length, $l_{cell} = l_b + l_s$, m
$l_{reactor}$ = reactor length, m
l_s = liquid slug length, m
L_b = dimensionless Taylor bubble length, l_b/d
$L_{reactor}$ = dimensionless $l_{reactor}$, $l_{reactor}/d$
L_s = dimensionless liquid slug length, l_s/d
$\mathbf{n}_b$ = interface unit normal vector
$\mathbf{n}_t$ = interface unit tangent vector
$\mathbf{N}$ = tracer flux, kg m^{-2} s^{-1}
p = relative pressure, N m^{-2}
Pe = bulk Peclet number, U_bd/D
$\bar{Q}$ = liquid volumetric flow rate into the unit cell, m^3/s
Q = dimensionless liquid volumetric flow rate into the unit cell, Q/U_bd^2
r_0 = radial position of vortex center, m
r_1 = radial position of streamline separating vortex and film regions in slug, m
$\bar{R}$ = microchannel dimensionless radius, $\frac{1}{2}$
Re = Reynolds number, $\rho U_bd/\mu$
s = variable of Laplace domain
Sp = cubic spline polynomial
Sh = Sherwood number, k_Ld/D
t = time, s
$\bar{t}$ = dimensionless time, tU_b/d
t_{cell} = time for a unit cell to move a length l_{cell}, l_{cell}/U_b, s
$t_{reactor}$ = time for a unit cell to pass through reactor, $l_{reactor}/U_b$, s
t_s = *CSTR* time constant, s
$\bar{t}_s$ = dimensionless *CSTR* time constant, V/A_fd
$\mathbf{u}$ = velocity field, ms^{-1}
u_z, u_r = radial and axial velocity components, ms^{-1}
U_b = bubble velocity, ms^{-1}
V = volume of slug, m^3
$\bar{V}$ = dimensionless volume of slug, V/d^3
V_1 = volume of slug film region, m^3
V_2 = volume of slug vortex region, m^3
Z_{1n} = nth zero of Bessel function of the first kind of order one

Greek letters

α, β, ε, ϕ = coefficients of spline polynomial
η, κ, θ, ζ = parameters for the two-region model see Eqs. 22–25
γ = interfacial tension, N m^{-1}
δ = thickness of film surrounding bubble, m
$\bar{\delta}$ = dimensionless film thickness, δ/d
$\bar{\lambda}_n$ = nth zero of the Bessel function of the first order
μ = viscosity, N s m^{-2}
μ_n = nth moment of $E(t)$
ρ = density, kg m^{-3}
σ = standard deviation of unit cell RTD, s
τ = space-time for unit cell, s
$\bar{\tau}$ = dimensionless space time, $\bar{V}/\bar{Q}$
τ_{cycle} = vortex cycle time, s
$\bar{\tau}_{\text{cycle}}$ = dimensionless vortex cycle time, $\tau U_b/d$
ψ = velocity ratio of bubble to average slug velocity

Superscripts

n = unit cell number
$\bar{x}$ = barred symbols are nondimensionalized

Subscripts

0 = Initial value at $t = 0$
av = average value in the slug
f = film
i = Inlet value
o = outlet value
v = vortex

Literature Cited

1. Thulasidas TC, Abraham MA, Cerro RL. Dispersion during bubble-train flow in capillaries. *Chem Eng Sci*. 1999;54:61–76.
2. Thulasidas TC, Abraham MA, Cerro RL. Flow patterns in liquid slugs during bubble-train flow inside capillaries. *Chem Eng Sci*. 1997;52:2947–2962.
3. Irandoust S, Andersson B. Mass-transfer and liquid-phase reactions in a segmented 2-phase flow monolithic catalyst reactor. *Chem Eng Sci*. 1988;43:1983–1988.
4. Irandoust S, Andersson B. Simulation of flow and mass-transfer in Taylor flow through a capillary. *Comp & Chem Eng*. 1989;13:519–526.
5. Berčic G, Pintar A. The role of gas bubbles and liquid slug lengths on mass transport in the Taylor flow through capillaries. *Chem Eng Sci*. 1997;52:3709–3719.
6. Berčic G. Influence of operating conditions on the observed reaction rate in the single channel monolith reactor. *Catalysis Today*. 2001;69:147–152.
7. Lucy CA, Hausermann BP. Co-current chromatography: A new mode of liquid-liquid chromatography. *Analytica Chimica Acta*. 1995;307:173–183.
8. Kreutzer M. *Hydrodynamics of Taylor flow in capillaries and monolith reactors*. Delft University; 2003. PhD thesis.
9. Yawalkar A, Sood R, Kreutzer M, Kapteijn F, Moulijn J. Axial mixing in monolith reactors: Effect of channel size. *Ind & Eng Chem Res*. 2005;44:2046–2057.
10. Khan S, Günther A, Schmidt M, Jensen K. Microfluidic synthesis of colloidal silica. *Langmuir*. 2004;20:8604–8611.
11. Günther A, Jhunjhunwala M, Thalmann M, Schmidt M, Jensen K. Micromixing of miscible liquids in segmented gas-liquid flow. *Langmuir*. 2005;21:1547–1555.
12. Trachsel F, Günther A, Khan S, Jensen K. Measurement of residence time distribution in microfluidic systems. *Chem Eng Sci*. 2005;60:5729–5737.
13. Tice J, Song H, Lyon A, Ismagilov R. Formation of droplets and mixing in multiphase microfluidics at low values of the Reynolds and the Capillary Numbers. *Langmuir*. 2003;19:9127–9133.
14. Skeggs LJ. An automatic method for calorimetric analysis. *Am J for Clinical Path*. 1957;28:311–322.
15. Amador C, Salman W, Sanguanpiyapan S, Gavriilidis A, Angeli P. Effect of gas-inlet conditions on the mechanism of Taylor flow formation in *Proceedings of the 5th International Conference on Multiphase Flow ICMF'04,* Yokohama, Japan: paper No. 515; 2004.
16. Serizawa A, Feng Z, Kawara Z. Two-phase flow in microchannels. *Experimental Thermal and Fluid Sci*. 2002;26:703–714.
17. Bretherton FP. The motion of long bubbles in tubes. *J of Fluid Mechanics*. 1961;10:166–188.
18. Nauman EB, Buffman BA. *Mixing in Continuous Flow Systems*. John Wiley & Sons, New York; 1983.
19. Thiers RE, Reed AH, Delander K. Origin of the lag phase of continuous-flow analysis curves. *Clinical Chem*. 1971;17:42–48.
20. Salman W, Gavriilidis A, Angeli P. A model for predicting axial mixing during gas-liquid Taylor flow in microchannels at low Bodenstein numbers. *Chem Eng J*. 2004;101:391–396.
21. Pedersen H, Hovarth C. Axial dispersion in a segmented gas-liquid flow. *Ind & Eng Chem Fund*. 1981;20:181–186.
22. Hovarth C, Solomon B, Engasser J. Measure of radial transport in slug flow using enzyme tubes. *Ind & Eng Chem Fund*. 1973;12:431–439.
23. Gruber R, Melin T. Radial mass transfer enhancement in bubble train flow. *Int J of Heat and Mass Transfer*. 2003;46:2799–2808.
24. Edvinsson RK, Irandoust S. Finite-element analysis of Taylor flow. *AIChE J*. 1996;42:1815–1823.
25. Giavedoni MD, Saita FA. The axisymmetrical and plane cases of gas phase steadily displacing a Newtonian liquid - A simultaneous solution of the governing equations. *Physics of Fluids*. 1997;9:2420–2428.
26. Giavedoni MD, Saita FA. The rear meniscus of a long bubble steadily displacing a Newtonian liquid in a capillary tube. *Physics of Fluids*. 1998;11:786–794.
27. Heil M. Finite Reynolds number effects in the Bretherton problem. *Physics of Fluids*. 2001;13:2517–2521.
28. Salman W. *Characterisation and Modeling of Taylor Flow in Small Circular Channels for the Purpose of Sequential Screening*. University College London, U.K.; 2005. PhD thesis.
29. Severino M, Giavedoni MD, Saita FA. A gas phase displacing a liquid with soluble surfactants out of a small conduit. *Physics of Fluids*. 2003;15:2961–2972.
30. Lide D. ed. *CRC Handbook of Chemistry and Physics*. CRC Press Inc. 85th ed., 2004.
31. COMSOL Inc. 1 New England Executive Park, Suite 350, Burlington, MA. 01803 *Femlab ver 2.3 software manual*; 2002.
32. Burden RL, Faires DJ, Reynolds AC. *Numerical Analysis*. Boston: Prindle, Weber, and Schmidt. Natural Cubic Spline Algorithm; 1978.
33. http://library.wolfram.com/infocenter/MathSource/699/. viewed 9/2003.
34. Valk PP, Abate J. Comparison of sequence accelerators for the Gaver method of numerical Laplace transform inversion. *Comp and Math with Applications*. 2003;48:629–636.
35. http://library.wolfram.com/database/MathSource/4738/. viewed 9/2003.

Manuscript received Apr. 12, 2006, and revision received Jan. 15, 2007, and final revision received Mar. 26, 2007.